ELSEVIER

Chemical Engineering Science 61 (2006) 4316–4331

Chemical Engineering Science

www.elsevier.com/locate/ces

Analysis of a cathode catalyst layer model for a polymer electrolyte fuel cell

P. Berg[a,*], A. Novruzi[b], K. Promislow[c]

[a] *Faculty of Science, UOIT, 2000 Simcoe Street N., Oshawa, Ont., Canada L1H 2K6*
[b] *Department of Mathematics and Statistics, University of Ottawa, 585 King Edward, Ottawa, Ont., Canada K1N 6N5*
[c] *Department of Mathematics, Michigan State University, East Lansing, MI 48824, USA*

Received 30 June 2005; received in revised form 20 January 2006; accepted 26 January 2006
Available online 29 March 2006

Abstract

A macroscopic model for a non-isothermal cathode catalyst layer (CL) in a proton exchange membrane (PEM) fuel cell is presented, in which liquid water in the CL pores is neglected. The model couples three phases: an electrically conductive carbon/platinum phase, gas pores, and a proton-conducting Nafion phase. The reaction–diffusion dynamics are described by a nonlinear system of differential equations which, due to the wide range of physical parameters, is very stiff. To reduce the stiffness of the system, an appropriate scaled model is introduced. A numerical algorithm consisting of two embedded Newton loops, specifically developed to handle the stiffness, is presented. Several numerical results are used to investigate the dynamics of the layer and the validity of the *interface reduction*, or zero CL thickness limit, which is often used in large fuel cell computations. In the limit of infinite water adsorption rate between ionomer phase and pore, a boundary layer emerges at either side of the CL, in which the water sorption equilibrium [Zawodzinski, T., Derouin, C., Radzinski, S., Sherman, R., Smith, V., Springer T., Gottesfeld, S., 1993. A comparative study of water uptake by and transport through ionomeric fuel cell membranes. Journal of the Electrochemical Society 140, 1981–1985] between ionomer and pore is violated.

PACS: 02.70.Dh; 47.11.+j; 47.70.Fw; 82.20.−w; 82.20.Wt; 82.45.Fk

Keywords: Catalysis; Electrochemistry; Mathematical modelling; Mass transfer; Catalyst layer; PEM fuel cell

1. Introduction

Fuel cells promise to deliver an environmentally benign future technology which yields highly efficient energy conversion (Serfass et al., 1994). In essence, hydrogen fuel cells combine hydrogen and oxygen in a spatially separated electrochemical reaction to produce electricity, with water being the only end product. There are many scientific, technological and engineering challenges to be solved in order to make fuel cells economically viable, efficient, reliable and durable under a wide range of operating conditions (Eikerling et al., 2005).

In this paper, a macro-homogeneous model for the competing processes in the cathode catalyst layer (CL) of a proton exchange membrane (PEM) fuel cell is presented. The layer is a very thin ($\approx 10\,\mu m$) three-phase medium, in which the electrochemical reaction takes place. It consists of (i) gas pores which supply oxygen and contain nitrogen, gaseous and liquid water, (ii) distributed ionomer (PEM) portions, a complex porous medium which adsorbs water and facilitates proton conduction, embedded in (iii) an agglomeration of carbon (electronic conductor) and platinum catalyst.

The CL must conduct electrons, protons, and oxygen to the active catalyst sites. The protons and electrons originate in the anode CL from the oxidation of hydrogen. The protons migrate across the charge selective membrane which separates anode from cathode, while the electrons flow through an external circuit from the anode to the cathode. Oxygen gas migrates from gas flow channels on the cathode side, through the gas diffusion layer (GDL), and into the CL. Thus the protons arrive from the polymer membrane side of Fig. 1 while the electrons and oxygen arrive from the backing layer (GDL). The oxygen is transported in the gas phase, the electrons in the conductive carbon

* Corresponding author. Tel.: +1 905 721 3111x2457; fax: +1 905 721 3304.
E-mail address: peter.berg@uoit.ca (P. Berg)
URL: http://www.peterberg.net (P. Berg).

0009-2509/$ - see front matter © 2006 Elsevier Ltd. All rights reserved.
doi:10.1016/j.ces.2006.01.033

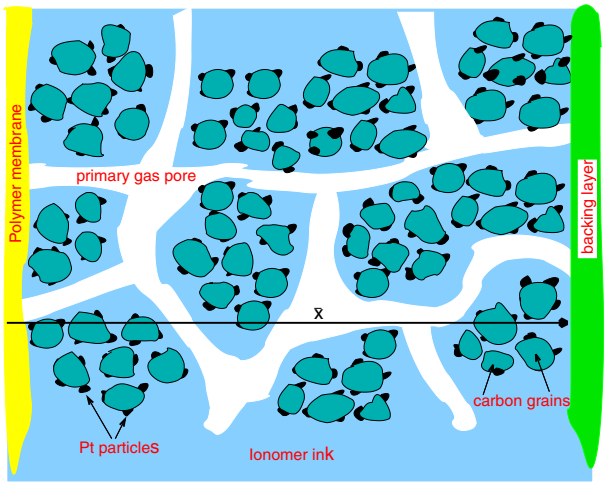

Fig. 1. The cathode catalyst layer is a three-phase medium consisting of a carbon/platinum phase (electronic conductor), the ionomer (protonic conductor) and gas pores (oxygen supply). This facilitates the half-cell reaction $O_2 + 4H^+ + 4e^- \rightarrow 2H_2O$. Water is present in both the ionomer and the pores. In macroscopic models, this intricate structure is modelled using a homogenized medium with average values and transport properties for all variables. In this paper, $\bar{x} = 0$ denotes the PEM–CL interface while $\bar{x} = \bar{l}$ denotes the CL–GDL interface.

phase, and the protons in the hydrated ionomer phase. The central question is, at given operating conditions, where within the CL the reaction takes place, and how is the reaction distribution sensitive to the operating conditions and CL composition.

CL models have recently received increasing attention (Eikerling et al., 2005; Pisani et al., 2003; Siegel et al., 2004). The models range in complexity from simplistic yet analytical (Eikerling et al., 2005) to comprehensive and complex (Pisani et al., 2003; Siegel et al., 2004). Eikerling et al. (2005) has modelled the impedance of the layer with only two effects, oxygen diffusion in the pores and ohmic losses in the PEM. This allows (by definition) for time dependency of the variables. This was later extended to cover agglomerate models including liquid water transport (Eikerling, 2006). A key question, which arises at the agglomerate level, is how mesoscopic pore level characteristics affect the transport characteristics at the macroscopic level, i.e., at the layer scale (Pisani et al., 2004; Wang et al., 2004). There exists an intricate interplay between porosity and pore size distribution on one side, and liquid water distribution and performance of the layer on the other side.

A very comprehensive CL model was suggested by Siegel et al. (2004). It draws particular attention to liquid water in the pores and predicts a large impact on the CL performance. However, the authors assume that the different phases in which water can be present, namely ionomer and pore (liquid and vapour) water, are at equilibrium. There are indications that this is not the case under fuel cell operation (Berg et al., 2004) and this problem forms part of this paper.

The comprehensive macro-homogeneous model considered in this paper describes a non-isothermal CL in a PEM fuel cell run with pure oxygen feed. Although liquid water in the pores plays a crucial role in the CL dynamics, it is neglected in this study. The main reason is that a model, void of liquid water in the pores, should be studied and analysed in detail first, before the poorly understood transport of liquid pore water is included. Only water in vapour form is considered in the pores. In addition, this approach is a good approximation when operating conditions entail low current densities and low humidity (Eikerling, 2006). In contrast, the ionomer can assume full saturation, thereby enhancing proton transport. The model couples the transport processes for the three phases:

(1) C/Pt (electric potential),
(2) pores (oxygen and water vapour concentrations, pressure), and
(3) ionomer (proton concentration, water content, electric potential).

The temperature is assumed to be the same for all three phases with heat transport dominated by the conduction in the carbon phase. Although the microscopic and mesoscopic structure of this complex medium plays a crucial role with respect to its performance characteristics (Eikerling, 2006; Pisani et al., 2003), this article will focus on macroscopic effects. The underlying structure enters the model through key parameters of the reactive medium.

The paper is organized as follows. First we present the model in Section 2, a reaction–convection–diffusion system, where diffusion is the dominating transport mode. To simplify the initial (dimensional) model, some reduction of the nonlinear diffusive coefficients and source terms is made. An appropriate scaling of variables leads to a better-conditioned system of nonlinear differential equations (NDE). The details of the scaling are presented to the interested reader in Appendix A. In addition, the computational results show that the numerical method, presented in Appendix B, is well suited for such kind of nonlinear problem. In fact, it represents a typical inverse problem with respect to the boundary value of one of the variables, the ionomer electric potential at the CL–PEM interface. In order to identify the contribution of different key parameters (e.g. rate of water evaporation from ionomer into pore, Berg et al., 2004) to the CL fluid dynamics, we have made a number of numerical simulations that we present in the second part of this paper (Section 3). Special attention is drawn to the *interface reduction* of the CL and the assumption of PEM water sorption equilibrium (isotherm) (Berg et al., 2004). A brief analysis of a boundary layer, which emerges from the numerical results, is given in Appendix C.

2. Model

In this section, a macro-homogeneous model is presented which treats the CL as a homogenized medium with average transport properties, described parametrically in the governing equations. These parameters depend intricately on the microscopic and mesoscopic structure of the layer (Eikerling, 2006; Pisani et al., 2003). However, the goal of this publication is not to relate the detailed structure of the medium to its macroscopic transport characteristics. The aim is to analyse the

coupling of the macroscopic transport processes and its impact on the functionality of the medium.

Following Fig. 1, we chose $\overline{x} \in (0, \overline{l})$ as the space variable, where $\overline{x} = 0$ denotes the membrane–CL interface and $\overline{x} = \overline{l}$ the CL–GDL interface.[1] The system equations describe the dynamics of the eight primary unknown variables

ionomer water content, $\overline{c}_w^m$,
ionomer electric potential, $\overline{\varphi}$,
temperature, $\overline{\tau}$,
pore gas pressure, $\overline{p}$,
pore vapour concentration, $\overline{c}_v$,
pore oxygen concentration, $\overline{c}_o$,
C/Pt electric potential, $\overline{U}$,
over-potential, $\overline{\eta}$,

for which we will need eight equations. In what follows, additional variables will be introduced but they are all dependent on the eight variables above and, therefore, not independent. The governing equations can be split into the three phases as follows, where we assume that the temperature is locally identical in all phases.

Ionomer: The primary variables of the ionomer are local water content $\overline{c}_w^m$, hydronium concentration $\overline{c}_+$, electric potential $\overline{\varphi}$ and temperature $\overline{\tau}$, governed by

$$\frac{\mathrm{d}}{\mathrm{d}\overline{x}}\left(-\overline{D}_w \frac{\mathrm{d}}{\mathrm{d}\overline{x}}\overline{c}_w^m\right) = \frac{3}{2}\overline{S}_c - \overline{\gamma}_{am}\overline{I}_w, \tag{1}$$

$$\frac{\mathrm{d}}{\mathrm{d}\overline{x}}\left(\overline{D}_+\left(-\frac{F}{\mathscr{R}\overline{\tau}}\overline{c}_+\frac{\mathrm{d}}{\mathrm{d}\overline{x}}\overline{\varphi} - \frac{\mathrm{d}}{\mathrm{d}\overline{x}}\overline{c}_+\right)\right) = -\overline{S}_c, \tag{2}$$

$$-\frac{\mathrm{d}}{\mathrm{d}\overline{x}}\left(\kappa_c \frac{\mathrm{d}}{\mathrm{d}\overline{x}}\overline{\tau}\right) = \left(\frac{\delta_s^c}{4}\overline{\tau} + F\overline{\eta}\right)\overline{S}_c - h_v\overline{\gamma}_{am}\overline{I}_w, \tag{3}$$

where $\mathrm{d}/\mathrm{d}\overline{x}$ denotes the gradient with respect to $\overline{x}$.

The ionomer phase carries water and protons. It consists of a hydrophobic polymer backbone to which, in case of Nafion, sulphonic acid groups (SO_3H) are attached. These acid groups form a local ion exchange equilibrium with the surrounding water molecules and hydronium ions (H_3O^+) (Berg et al., 2004) as the protons dissociate:

$$SO_3H + H_2O \leftrightarrow SO_3^- + H_3O^+ \tag{4}$$

Assuming local electro-neutrality, this ion exchange equilibrium leads to a local hydronium concentration $\overline{c}_+$ as a function of the water concentration of the ionomer (Berg et al., 2004)

$$\overline{c}_+ := \overline{c}_+(\overline{c}_w^m) = -\frac{k_H}{2}\overline{c}_w^m + \left(\frac{1}{4}(k_H\overline{c}_w^m)^2 + k_H a\overline{c}_w^m\right)^{1/2}. \tag{5}$$

Hydronium electro-diffuses across the ionomer, driven by concentration gradients and the electric field. Reflecting a fundamental property of ion-exchange membranes, concentration gradients exist although the ionomer is electro-neutral (Paddison et al., 2000). Electro-diffusion is typically described by the Nernst–Planck equation (2), where a local sink term $\overline{S}_c$, the so-called Butler–Volmer equation (see detailed discussion below), arises due to the half-cell reaction

$$O_2 + 4H_3O^+ + 4e^- \rightarrow 6H_2O \tag{6}$$

Effectively, we consider a water drag coefficient equal to one since protons are assumed to flow only as hydronium, whose concentration is denoted by $\overline{c}_+$. The water profile through the ionomer phase is thus described by Eq. (1), where an explicit water drag coefficient can be omitted since the water drag (equal to one) has been incorporated into the transport equation (2) for hydronium (Berg et al., 2004). The water diffusion through the ionomer is nonlinear, with a diffusion coefficient that depends linearly on the water concentration (Berg et al., 2004). This reflects the changing pore structure and pore connections of the PEM with water content. The source term S_c for water is based on the usual assumption that water is produced at the catalyst surface in the ionomer phase.

The $\overline{I}_w$ term, defined by

$$\overline{I}_w = \overline{c}_w^m - \overline{c}_w^*, \tag{7}$$

describes the deviation from water sorption equilibrium at the interface between ionomer and gas phase, and is set to be proportional to the water flux across that interface (Berg et al., 2004). When no current is drawn, we find $\overline{I}_w = 0$. Then $\overline{c}_w^m = \overline{c}_w^*$ and the ionomer water content $\overline{c}_w^m$ is solely determined by the relative humidity r in the gas pores via

$$\overline{c}_w^* := \overline{c}_w^*(\overline{\tau}, \overline{c}_v) = a(0.3 + 10.8r - 16r^2 + 14.1r^3). \tag{8}$$

This equation is, therefore, called *water sorption isotherm* and its shape has been measured for various types of PEM by several researchers (Zawodzinski et al., 1993). In this paper, Eq. (8) describes the water sorption isotherm of bulk Nafion and must, therefore, be considered as a qualitative rather than quantitative relationship. Note that for an isolated membrane, it takes between 10 and 1000 s to reach that equilibrium.

In our averaged model not all elements of the ionomer are in contact with the gas phase, and thus it is inappropriate to impose the equilibrium water sorption condition $\overline{c}_w^m = \overline{c}_w^*$ when a current is drawn. However, the water sorption could be near equilibrium, given by $\overline{c}_w^*$, even though the whole system is not in equilibrium under stationary fuel cell operation, as long as the time scale for water sorption and diffusion within the PEM are sufficiently small as compared to the time scale of water production (Berg et al., 2004). Therefore, we impose that the exchange of water between ionomer and gas phase is proportional to the disequilibrium (7). The constant of proportionality $\overline{\gamma}_{am}$, a water adsorption rate coefficient, scales like

$$\overline{\gamma}_{am} \sim \frac{D_e\beta}{\overline{d}}, \tag{9}$$

where D_e is an effective water diffusivity, β is a local surface area density (m^2/m^3) and $\overline{d}$ is an average distance of points in the ionomer phase to an ionomer–gas pore interface. In this

[1] Throughout this paper, an overlined variable denotes a dimensional variable, while a non-overlined variable generally denotes a dimensionless variable.

paper, we choose $\overline{\gamma}_{am} = 5.7\,\mathrm{s}^{-1}$, which is several orders of magnitude smaller than what Pisani et al. (2003) used. Note that as $\overline{\gamma}_{am} \to \infty$, $\overline{c}_w^m$ approaches $\overline{c}_w^*$, corresponding to sorption equilibrium. The sensitivity of the model to this key parameter will be analysed in Section 3 and in the Appendix.

Finally, we assume that temperature is identical in all three phases (see Eq. (3)). Linear heat transfer is governed by reversible and irreversible heat generation in the reaction (term $\sim \overline{S}_c$), and evaporative cooling when a water flux $\overline{\gamma}_{am}\overline{I}_w$ leaves the ionomer and enters the pore.

Gas pore: The three equations needed are conservation of mass in the pore (Eq. (10)), with a local sink term due to water adsorption of the ionomer and oxygen consumption in the reaction, and convection–diffusion transport of oxygen (Eq. (12)) and water vapour (Eq. (11)), with corresponding source terms. Note that liquid water is not modelled in the gas pore phase. For the chosen parameters of this model, diffusion is the dominant gas transport effect and convection plays only a minor role due to the small permeability of gas pores (Stumper et al., 2005). In fact, gas transport in CL gas pores is often modelled by Knudsen diffusion (Stumper et al., 2005). We will see in the results section, however, that convection is not negligible altogether.

$$\frac{\mathrm{d}}{\mathrm{d}\overline{x}}(\overline{\rho}\,\overline{u}) = \overline{\gamma}_{am} M_v \overline{I}_w - \frac{M_o}{4}\overline{S}_c, \tag{10}$$

$$\frac{\mathrm{d}}{\mathrm{d}\overline{x}}\left(-\overline{D}_v \overline{\mathbf{c}}\frac{\mathrm{d}}{\mathrm{d}\overline{x}}\left(\frac{\overline{c}_v}{\overline{\mathbf{c}}}\right) + \overline{c}_v\overline{u}\right) = \overline{\gamma}_{am}\overline{I}_w, \tag{11}$$

$$\frac{\mathrm{d}}{\mathrm{d}\overline{x}}\left(-\overline{D}_o \overline{\mathbf{c}}\frac{\mathrm{d}}{\mathrm{d}\overline{x}}\left(\frac{\overline{c}_o}{\overline{\mathbf{c}}}\right) + \overline{c}_o\overline{u}\right) = -\frac{1}{4}\overline{S}_c. \tag{12}$$

Here, $\overline{D}_o = \overline{D}_v$ holds because we have a binary mixture.

Carbon/Pt: The electric potential of the carbon phase follows Ohm's law with a sink term due to electron consumption in the reaction. It is related to the local over-potential $\overline{\eta}$, equilibrium electrode potential E_o and ionomer potential $\overline{\varphi}$ (Berg et al., 2004).

$$\overline{\sigma}_c \frac{\mathrm{d}^2}{\mathrm{d}\overline{x}^2}\overline{U} = -F\overline{S}_c, \tag{13}$$

$$\overline{\eta} = E_o - \overline{U} + \overline{\varphi}. \tag{14}$$

The remaining (dependent) variables are explained in Table 1 and in Eqs. (15)–(23).

$$\overline{D}_w = \frac{d_w}{a}\overline{c}_w^m \mathrm{e}^{-2436/\overline{\tau}}, \tag{15}$$

$$\overline{D}_+ = \frac{d_+}{a}\overline{c}_w^m \mathrm{e}^{-1663/\overline{\tau}}, \tag{16}$$

$$\overline{\mathbf{c}} = \overline{c}_v + \overline{c}_o, \tag{17}$$

$$\overline{S}_c = \frac{\overline{\sigma}_{pm} i_{0,c}}{F c_{o,\mathrm{ref}}}\left(\frac{\overline{c}_+}{a}\right)^{e_c}(\overline{c}_o - \overline{\delta}\,\overline{S}_c)\exp\left(\frac{F}{2\mathscr{R}}\frac{\overline{\eta}}{\overline{\tau}}\right),$$

$\overline{\delta}, \overline{\sigma}_{pm} > 0$; it follows that

Table 1
List of main parameters and dependent variables

	Variable	Unit
$\overline{c}_w^m$	ionomer water conc.	$\mathrm{mol/m^3}$
$\overline{\varphi}(\overline{\phi})$	ionomer potential (in plots)	V
$\overline{\tau}$	temperature	K
$\overline{u}$	velocity	m/s
$\overline{c}_v$	vapour molar con.	$\mathrm{mol/m^3}$
$\overline{\mathbf{c}}$	total gas molar conc.	$\mathrm{mol/m^3}$
$\overline{\eta}$	over-potential	V
$\overline{c}_+$	ionomer proton conc.	$\mathrm{mol/m^3}$
$\overline{\varphi}_0$	GDL/CL potential	V
$\overline{p}$	gas pressure	Pa
$\overline{\rho}$	density	$\mathrm{kg/m^3}$
$\overline{c}_o$	oxygen molar conc.	$\mathrm{mol/m^3}$
$\overline{U}$	carbon phase potential	V
$\overline{S}_c$	reaction rate	$\mathrm{mol/(m^3\,s)}$

$$\overline{S}_c = \frac{\overline{\sigma}_{pm} i_{0,c}}{F c_{o,\mathrm{ref}}}\left(\frac{\overline{c}_+}{a}\right)^{e_c}\overline{c}_o \exp\left(\frac{F}{2\mathscr{R}}\frac{\overline{\eta}}{\overline{\tau}}\right) \times\left(1 + \overline{\delta}\frac{\overline{\sigma}_{pm} i_{0,c}}{F c_{o,\mathrm{ref}}}\left(\frac{\overline{c}_+}{a}\right)^{e_c}\exp\left(\frac{F}{2\mathscr{R}}\frac{\overline{\eta}}{\overline{\tau}}\right)\right)^{-1}, \tag{18}$$

$$r = \frac{\mathscr{R}}{101300}\overline{c}_v\overline{\tau}\;10^{-Q(\overline{\tau})}, \tag{19}$$

$$Q(\overline{\tau}) = -2.18 + 0.029(\overline{\tau} - 273.2) - 9.18\times10^{-5} \times(\overline{\tau} - 273.2)^2 + 1.44\times10^{-7}(\overline{\tau} - 273.2)^3, \tag{20}$$

$$\overline{p} = \mathscr{R}\overline{\tau}\overline{\mathbf{c}}, \tag{21}$$

$$\overline{u} = -\frac{K}{\mu}\frac{\mathrm{d}}{\mathrm{d}\overline{x}}\overline{p}, \tag{22}$$

$$\overline{\rho} = M_v\overline{c}_v + M_o\overline{c}_o + M_n\overline{c}_n \quad (\text{using } \overline{p} = \mathscr{R}\overline{\tau}\overline{\mathbf{c}}) = (M_v - M_n)\overline{c}_v + (M_o - M_n)\overline{c}_o + \frac{M_n}{\mathscr{R}}\frac{\overline{p}}{\overline{\tau}}. \tag{23}$$

Eq. (15) describes nonlinear ionomer water diffusion and (16) nonlinear hydronium diffusion.

Eq. (18), the *Butler–Volmer equation*, is the local reaction rate as a function of hydronium and oxygen concentration as well as over-potential. Note that we introduced a term $(\overline{c}_o - \overline{\delta}\,\overline{S}_c)$ which corresponds to the oxygen concentration at the agglomerate catalyst (Pt) sites, when the pore concentration is $\overline{c}_o$. This reflects the transport losses of oxygen between pore and reaction sites and leads to a limiting local reaction rate which cannot exceed $\overline{S}_c = \overline{c}_o/\overline{\delta}$. The relation between the agglomerate structure and the effective Butler–Volmer equation has been investigated by Pisani et al. (2003) and enters the model through the parameter $\overline{\sigma}_{pm}$, an effective interface density (interface area per volume). Also, we used the fact that at large cathode over-potentials, the dependency of the local reaction rate on the over-potential can be approximated by the reduction rate of oxygen

alone, i.e., $S_c \sim \exp[F\overline{\eta}/(2\mathscr{R}\overline{\tau})]$. This is a common assumption in fuel cell modelling and a very good approximation for the fuel cell operating conditions under consideration ($\overline{\eta} > 0.25\,\mathrm{V}$) so that deviations are negligible.

Eq. (21) is the ideal gas law and (22) Darcy's law.

Eqs. (1)–(14) are equipped with the following boundary conditions imposed on the membrane–CL interface $\overline{x} = 0$, and on the GDL–CL interface $\overline{x} = \overline{l}$:

$$\begin{cases} \overline{c}_w^m(0) = \text{given}, & \dfrac{\mathrm{d}}{\mathrm{d}\overline{x}}\overline{c}_w^m(\overline{l}) = 0, \\ \overline{\varphi}(0) = \varphi_0, & \dfrac{\mathrm{d}}{\mathrm{d}\overline{x}}\overline{\varphi}(\overline{l}) = 0, \\ \dfrac{\mathrm{d}}{\mathrm{d}\overline{x}}\overline{\tau}(0) = \overline{\alpha}\,\overline{\tau}(0), & \overline{\tau}(\overline{l}) = \text{given}, \\ \dfrac{\mathrm{d}}{\mathrm{d}\overline{x}}\overline{p}(0) = 0, & \overline{p}(\overline{l}) = \text{given}, \\ \dfrac{\mathrm{d}}{\mathrm{d}\overline{x}}\overline{c}_v(0) = 0, & \overline{c}_v(\overline{l}) = \text{given}, \\ \dfrac{\mathrm{d}}{\mathrm{d}\overline{x}}\overline{c}_o(0) = 0, & \overline{c}_o(\overline{l}) = \text{given}, \\ \dfrac{\mathrm{d}}{\mathrm{d}\overline{x}}\overline{U}(0) = 0, & \overline{U}(\overline{l}) = \text{given}. \end{cases} \tag{24}$$

In this model, oxygen is not entering the PEM. Moreover, ionomer water can only enter the CL pores but not the GDL pores.

Here, $\overline{\alpha}$ is a given constant and φ_0, the ionomer potential, is determined so that the prescribed total current I_t satisfies

$$F\int_0^{\overline{l}} \overline{S}_c\,\mathrm{d}\overline{x} = I_t. \tag{25}$$

For given values of the variables at the boundaries of the CL, the system is entirely determined by the value φ_0 of the ionomer potential at the PEM–CL interface, thus defining the solution $\mathbf{v} = \mathbf{v}(\varphi_0)$. In turn, φ_0 is defined by imposing the total current. This implies that the numerical solution results in two iterative methods, namely solving the system for a given φ_0, then iterating on φ_0 until the total current is matched. Each iterative method solves a nonlinear problem, and a Newton method is used for each of them (see also Appendix B).

3. Numerical results

The numerical code presented in Appendix B is used to identify the sensitivity of the model to the oxygen concentration at the CL–GDL interface $\overline{c}_o(\overline{l})$, the mass transfer parameter $\overline{\delta}$ for oxygen transport within the agglomerates, the hydration level of the ionomer, and the water transfer rate $\overline{\gamma}_{am}$ between ionomer and gas phases.[2] The key question addressed in this section is whether the *interface reduction* is a good approximation, i.e., whether the CL can be approximated well by an interface between PEM and GDL. This approach is often taken in large three-dimensional fuel cell computations without justification. Further goals are to investigate how $\overline{\gamma}_{am}$ affects the water profile (ionomer and pore) of the layer, and how the maximum current depends on $\overline{\delta}$ and $\overline{c}_o(\overline{l})$ (Tables 1 and 2).

Table 2
Material parameters

	Value	Unit
F	96 485	C/mol
a	1200	mol/m^3
δ_s^c	546.7	J/(mol K)
d_w	2.1×10^{-7}	m^2/s
h_v	4.52×10^4	J/mol
$\mathbf{c}_r$	100	mol/m^3
μ	2.2×10^{-5}	kg/(m s)
M_v	0.018	kg/mol
M_n	0.028	kg/mol
I_t		A/cm^2
$\overline{\gamma}_{am}$	5.7	s^{-1}
E_o	1.0	V
$\overline{l}$	10^{-5}	m
d_+	1.6×10^{-8}	m^2/s
τ_r	354	K
K	10^{-12}	cm^2
$\mathscr{R}$	8.31	J/(K mol)
M_o	0.032	kg/mol
$\overline{\sigma}_c$	3	S
$\overline{\delta}$	5×10^{-4}	s

3.1. Reference case

Since it is rather difficult to estimate precisely each physical parameter and coefficient of the model, such as oxygen diffusion coefficient or ionomer conductivity in the CL, we take a slightly different approach from the usual CL modelling work found in the literature. We define a reference case, shown in Fig. 2, to which all other results are compared. This allows us to better understand the dynamics of the layer and the impact of each individual parameter variation.

We observe the following notable features in the numerical data (top left to bottom right): The ionomer water c_w^m usually flows from GDL (no-flux boundary condition, i.e., zero gradient) towards the PEM. This is expected when the anode is rather dry, reflected here by the boundary value $c_w^m(0)$. The hydronium concentration c_+ follows c_w^m via (5) and is similar in shape. This means that the electric field really drives the hydronium ions from PEM towards GDL, against their concentration gradient. The pressure $\overline{p}$ is almost constant and convection plays only a minor role. The over-potential $\overline{\eta}$ varies by less than 0.02 V. The gradients of water vapour $\overline{c}_v$ and oxygen $\overline{c}_o$ are of opposite signs as expected in a binary mixture, with zero flux at the PEM interface. The model exhibits a typical monotonic shape for the reaction rate $\overline{S}_c$, with the maximum at the GDL interface. This is due to the decreasing oxygen concentration towards the PEM (Litster and McLean, 2004; Song et al., 2004). It is also noteworthy that $\overline{I}_w$ can change sign across the layer. This means that in some parts the water is adsorbed from the pores into the ionomer phase, and in other parts it evaporates from the ionomer into the pore (see Fig. 3). This fine

[2] It shall be pointed out once more that throughout this section, overlined variables and parameters are dimensional, whereas non-overlined quantities are dimensionless.

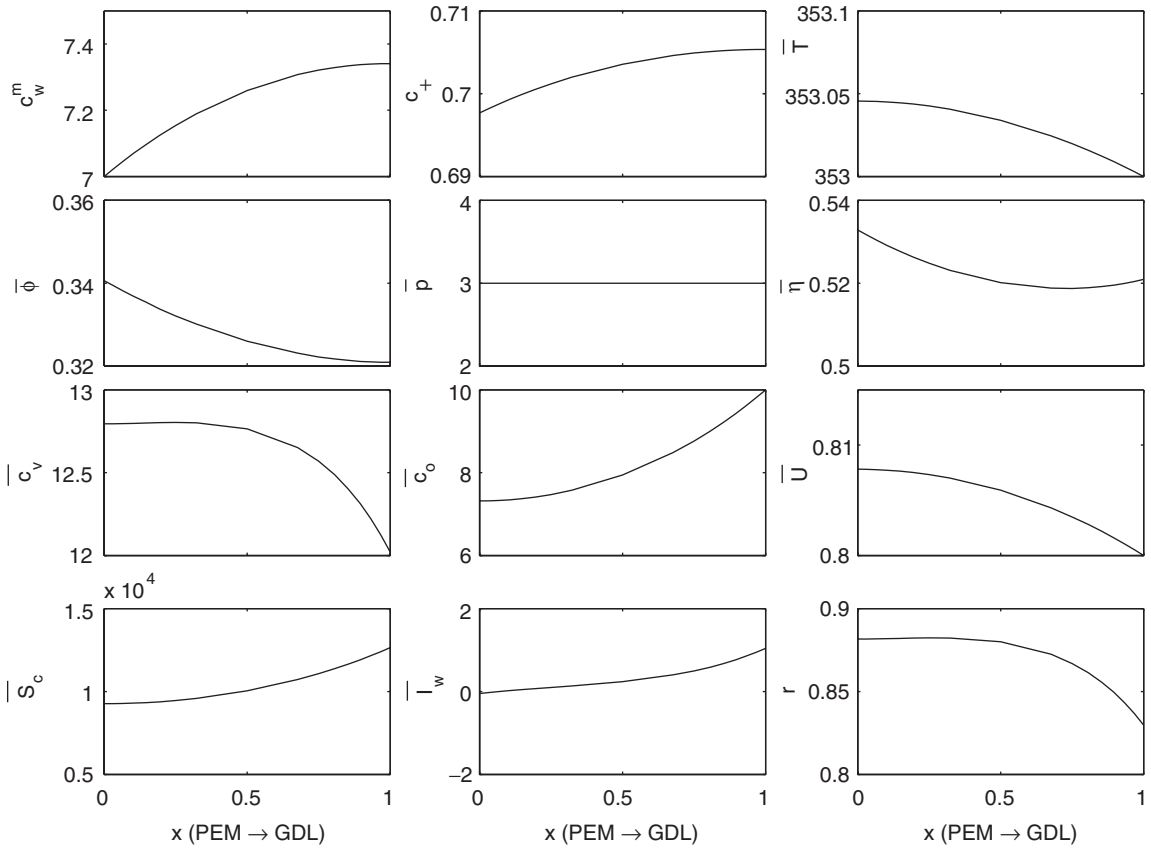

Fig. 2. Reference case: total current $I_t = 1.0\,\mathrm{A/cm^2}$, $c_w^m(0) = 7.0$, $\overline{\tau}(\bar{l}) = 353\,\mathrm{K}$, $\overline{p}(\bar{l}) = 3 \times 10^5\,\mathrm{Pa}$, $\overline{c}_v(\bar{l}) = 12\,\mathrm{mol/m^3}$, $\overline{c}_o(\bar{l}) = 10\,\mathrm{mol/m^3}$, $\overline{U}(\bar{l}) = 0.8\,\mathrm{V}$ (an arbitrary constant).

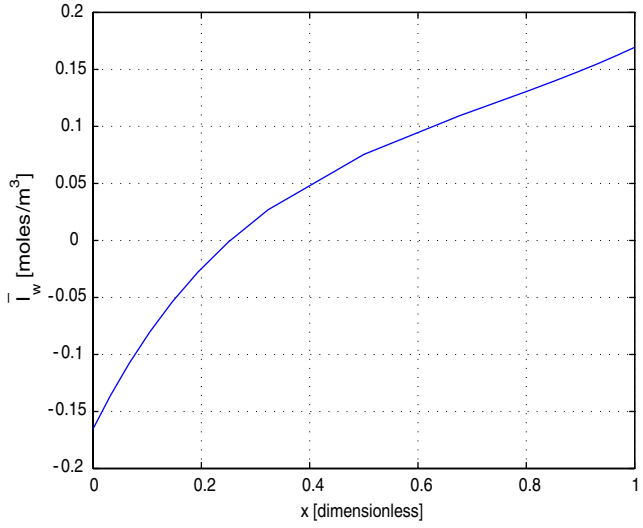

Fig. 3. The water flux between ionomer and pores can change signs across the layer. All parameters as in reference case except $c_w^m(0) = 6.0$.

balance depends very sensitively on all remaining variables of the system through the boundary conditions, which is symptomatic for the intricate nature of the water management of the medium.

Generally, the following variations across the layer are found for a given set of parameters and boundary conditions:

- ionomer water concentration $\overline{c}_m^w$: $< 10\%$;
- ionomer proton concentration $\overline{c}_+$: $< 2\%$;
- temperature $\overline{\tau}$ (also denoted by $\overline{T}$): $< 0.1\,\mathrm{K}$;
- pressure $\overline{p}$: negligible variation;
- ionomer potential $\overline{\varphi}$ (also denoted by $\overline{\phi}$): $< 0.05\,\mathrm{V}$;
- carbon phase potential $\overline{U}$: $< 0.02\,\mathrm{V}$;
- vapour concentration $\overline{c}_v$: $< 10\%$;
- oxygen concentration $\overline{c}_o$: up to 50% (at maximum currents);
- local reaction rate $\overline{S}_c$: up to 50% (at very high currents only).

Note that the variations for the vapour concentration are smaller than those for oxygen (even though it is a binary mixture) because water can be transported in the ionomer phase also. The water fluxes in pores and ionomer are coupled. This is reflected by a non-vanishing ionomer water flux at the PEM interface (in contrast to a zero-flux condition for oxygen) and a non-vanishing water vapour flux in the pores at the GDL interface. Also, convection is small but not negligible.

These observations lead to the conclusion that a simplified CL model might be sufficient which neglects variations in proton concentration, gas pressure and, possibly, electric potential

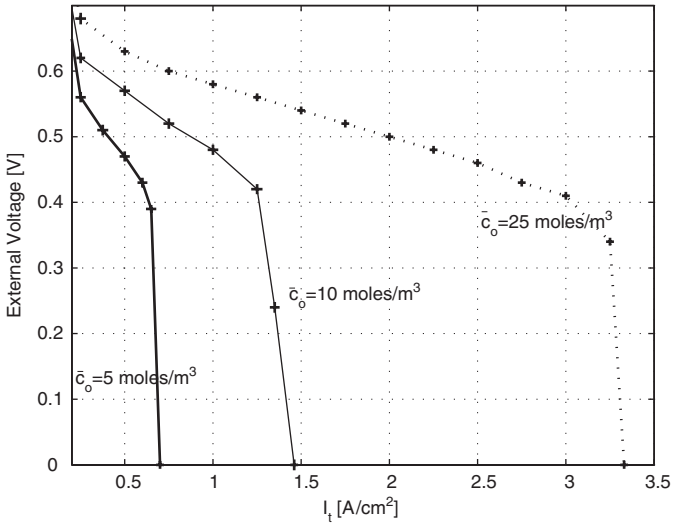

Fig. 4. Polarization curve for three different oxygen concentrations at the GDL–CL interface. For $\bar{c}_o = 10$ and $25\,\mathrm{mol/m^3}$, three regimes of voltage losses can be identified: kinetic regime, ohmic losses, mass transport losses. The latter define ultimately the maximum current.

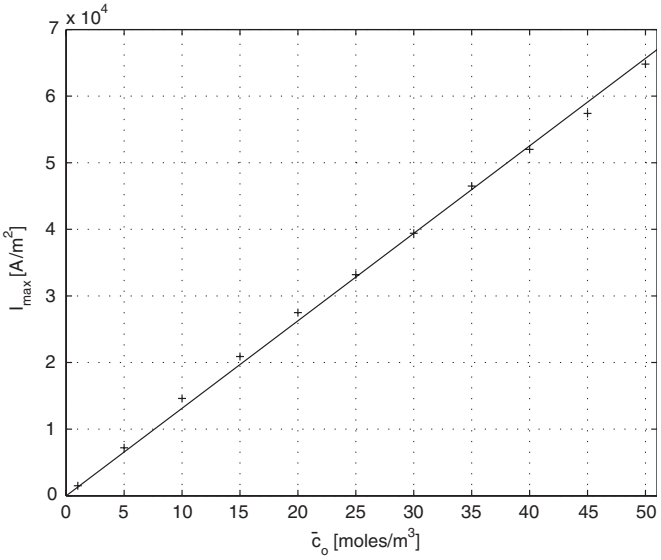

Fig. 5. The maximum current $I_{\max}$ as a function of the oxygen concentration at the CL–GDL interface: a linear scaling emerges. All other parameters as for the reference case.

of the carbon phase. Thermal variations might be important though when liquid water is included in the model. The derivation of such a model is planned future work.

3.2. Polarization curve

The most important macroscopic feature of the CL is the voltage loss U_{ext} across the layer described by $U_{\mathrm{ext}} = E_o - \overline{U}(0) + \overline{\eta}(1)$, as a function of the current drawn, I_t. The losses vanish when no current is drawn ($E_o = \overline{U}(0) - \overline{\eta}(1)$). This functional relationship is called the *polarization curve* and is illustrated in Fig. 4. This curve is particularly important for the overall fuel cell performance because each point on the curve (I_t, U_{ext}) also defines the power output of the device:

$$P = U_{\mathrm{ext}} I_t. \tag{26}$$

The shape of the polarization curve depends strongly on the operating conditions, for example, humidification level and oxygen pressure. The plot exhibits three curves for three different oxygen concentrations at the CL–GDL interface. This clearly shows that high oxygen concentration, typical for pure oxygen feed, leads to better performance of the fuel cell.

There are *three characteristic regimes* for each polarization curve. For small current densities I_t, the external voltage drops rapidly in an exponential fashion from the equilibrium electrode potential E_o ($E_o = 1.0\,\mathrm{V}$), governed by the exponential terms in the Butler–Volmer equation (18). This effect is solely determined by the microscopic reaction kinetics at the catalyst sites of the layer. Adjacent we find an intermediate linear regime where the voltage losses are mainly due to ohmic losses within the ionomer and carbon phase. In reality, most of these losses actually occur in the PEM, which explains the smaller than expected slope in Fig. 4. Finally, the external voltage drops off rapidly. The shape of this drop-off is referred to as the *knee* of the polarization curve. This feature arises due to mass transport losses of oxygen between pore and reaction sites. As the oxygen concentration at the reaction sites, $\overline{c}_o - \overline{\delta}\,\overline{S}_c$, approaches zero, the over-potential $\overline{\eta}$ in the Butler–Volmer equation increases rapidly. This effect is enhanced in fuel cells by the decreasing oxygen concentration at the CL–GDL interface when a current is drawn (Berg et al., 2004), since oxygen has to diffuse from channel to CL. The maximum oxygen reduction driven current (see also next section) is reached when $U_{\mathrm{ext}} = 0$, i.e., when the external voltage of the device vanishes. This is not necessarily equivalent to the limiting current found when the total current does not vary with the external voltage, $\mathrm{d}I_t/dU_{\mathrm{ext}} = 0$.

3.3. Maximum current

As mentioned in the previous section, the maximum current $I_{\max}$ is defined by the value of I_t at which $U_{\mathrm{ext}} = 0$. This value depends strongly on the operating conditions. We will look at the impact of two operating parameters in our model: (i) the oxygen concentration at the CL–GDL interface $\overline{c}_o(\bar{l})$ and (ii) the mass transfer parameter of oxygen transport within the agglomerates $\overline{\delta}$.

Fig. 5 exhibits a linear scaling of the maximum current with $\overline{c}_o(\bar{l})$. Although this might be expected from the linear oxygen dependency of the local reaction rate in the Butler–Volmer equation (18), it is not a trivial result since the oxygen concentration varies significantly (about 50%) across the CL at maximum currents. The plot shows why higher gas pressure, and hence higher oxygen concentration, leads to higher maximum currents and better performance. However, this is at the cost of gas compression and its related energy consumption which, in turn, leads to a trade-off in overall efficiency.

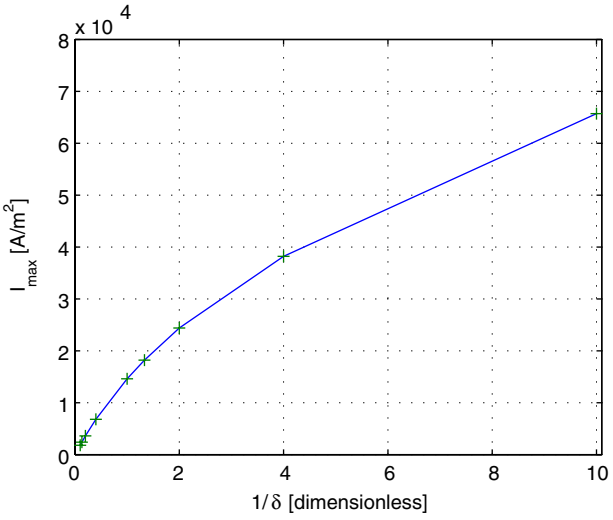

Fig. 6. The maximum current $I_{\max}$ as a function of the inverse mass transfer parameter $1/\delta$ normalized by the reference value $\overline{\delta}$: the scaling deviates from linear behaviour due to the variations of the variables across the catalyst layer. All other parameters as for the reference case.

The relationship between maximum current $I_{\max}$ and $1/\delta$ is shown in Fig. 6, where δ is normalized by the reference value used in Fig. 2. This transport parameter is linked to the mesoscopic transport processes of oxygen at the agglomerate level. Therefore, the structure and functionality of the CL at that scale is of very high importance (Pisani et al., 2003). As $\delta \to 0$ and so $1/\delta \to \infty$, the maximum current reaches exceedingly unrealistic values, unseen in experiments. On the other hand, increasing δ, i.e., $1/\delta \to 0$, pushes $I_{\max}$ towards zero. Note that $1/\delta$ corresponds to the effective diffusivity of oxygen within the agglomerates.

This near linear scaling of $I_{\max}$ with $1/\delta$, equivalent to a hyperbolic relationship between $I_{\max}$ and δ, is contained in the Butler–Volmer equation (18) for given oxygen concentration $\overline{c}_o$. For $\overline{\delta} \to 0$, $\overline{\eta} \to \infty$ implies $\overline{S}_c \to \infty$. The limit $\overline{\delta} \to \infty$, however, leads to $\overline{S}_c \sim \overline{c}_o/\overline{\delta} \to 0$ as $\overline{\eta} \to \infty$. The relationship between $I_{\max}$ and δ would be exactly inversely proportional if all variables were constant across the layer. Deviations from this trivial case, however, arise as the current drawn ($I_t = I_{\max}$) increases. This underlines the difference between finite and zero layer thickness, which will be discussed next in more detail.

3.4. Interface reduction

In many fuel cell models, the CL is treated as an interface. In the context of this model, there are three ways of looking at the "zero thickness" limit:

(1) Taking the limit $l \to 0$, keeping all other parameters fixed. This limit is unphysical since, for a given current, $\overline{\eta} \to \infty$ as $l \to 0$ and the maximum current, determined by $\overline{\eta} = E_o$, is reached very quickly. This gives a minimum CL thickness $l_{\min}$, below which a prescribed current cannot be drawn.

(2) Taking the limit $l \to 0$ and scaling $\overline{\delta} \to l\overline{\delta}$, $\overline{\gamma}_{am} \to \overline{\gamma}_{am}/l$ and $\overline{\sigma} \to \overline{\sigma}/l$ at the same time, as suggested in Appendix A.
Physically, this corresponds to compressing the layer along the through-plane to zero thickness, leaving an interface between GDL and PEM. To leading order, all variables become constants prescribed by the boundary conditions. The full model reduces to a set of boundary conditions for the PEM and GDL, respectively. The next-order correction to this trivial model is planned future work.

(3) Choose a finite l and see whether the full solution of the model could be represented by an interface.
This is what is effectively done in much research in the literature and we will now investigate whether this reduction is justified.

The Butler–Volmer equation for the reaction rate at a GDL–PEM interface usually takes the form (Berg et al., 2004)

$$\overline{S} = I_{\text{eff}}\, c_+ \overline{c}_o \exp\left(\frac{F\overline{\eta}}{2\mathscr{R}\overline{\tau}}\right), \tag{27}$$

with an (effective) exchange current density I_{eff}, taken to be constant across the whole range of operating conditions. Note that here the units of $\overline{S}$ are $\text{mol}/\text{m}^2/\text{s}$.

Following this idea, we will now analyse how the effective exchange current density I_{eff}, derived from the local current density I_t, the proton and oxygen concentration, and the overpotential via

$$I_{\text{eff}} = \frac{I_t}{c_+ \overline{c}_o \exp(F\overline{\eta}/2\mathscr{R}\overline{\tau})}, \tag{28}$$

varies with I_t. Fig. 7 exhibits this dependency. This is a test whether our more complex CL model can be replaced by an

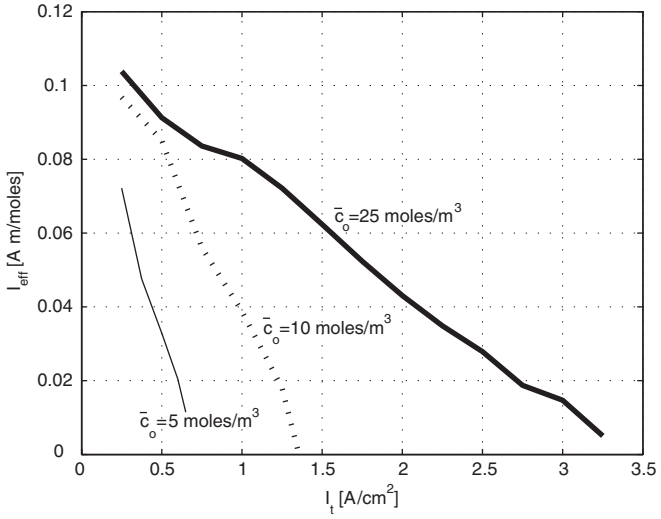

Fig. 7. Variation of the effective exchange current with total current and CL–GDL interface oxygen concentration. Except I_t and $\overline{c}_o(\overline{l})$, all parameters as in the reference case.

interface condition (27). The values needed in Eq. (28) are taken at the CL–GDL interface. Only if I_{eff} remains unchanged when operating conditions, i.e., boundary conditions, are varied can the CL dynamics be reduced to an interface. This is surely the case if all variables were constant across the layer, which will be referred to as the first-order approximation in what follows.

For large oxygen concentrations ($\overline{c}_o(\bar{l}) = 25\,\text{mol/m}^3$), as can be found for pure oxygen feed (Berg et al., 2005), I_{eff} varies with I_t by one order of magnitude. For smaller $\overline{c}_o(\bar{l})$, typical for air feed ($\overline{c}_o(\bar{l}) = 10\,\text{mol/m}^3$) (Berg et al., 2004), a similar variation of the effective exchange current is observed. Moreover, changing $\overline{c}_o(\bar{l})$ at $I_t = 0.5\,\text{A/cm}^2$, I_{eff} varies by about 200% (between 0.03 and 0.09 A/(m mol)). However, these results depend sensitively on the oxygen diffusion coefficient $\overline{D}_o$ and variations are more pronounced as $\overline{D}_o$ decreases. Therefore, it is critical to obtain an accurate estimate for this parameter which is estimated to be $\overline{D}_o = 5.0 \times 10^{-8}\,\text{m}^2/\text{s}$, following literature values (Eikerling, 2006; Stumper et al., 2005). This is a factor of 40 smaller than diffusion in the GDL, $D_o^g \approx 2.0 \times 10^{-6}\,\text{m}^2/\text{s}$, due to the small pore size in the CL. In essence, if it is at least an order of magnitude smaller than the GDL oxygen diffusion coefficient, I_{eff} can vary significantly and the assumption that the CL can be approximated by one interface for all types of operating conditions is likely to be invalid. This effect will also be enhanced by the incorporation of liquid pore water.

3.5. Over-potential vs. exchange current

We will now investigate another scaling between two parameters of the system. If the exchange current density $i_{o,c}$ is decreased, $\overline{\eta}$ must increase in order to match the same total current I_t. Using the Butler–Volmer equation

$$\overline{S} = i_{o,c}\, c_+\, c_o \exp\left(\frac{F\overline{\eta}}{2\mathscr{R}\overline{\tau}}\right) \tag{29}$$

and keeping all parameters fixed but $i_{o,c}$ and $\overline{\eta}$, a first-order approximation would be

$$i_{o,c} \exp\left(\frac{F\overline{\eta}}{2\mathscr{R}\overline{\tau}}\right) = \text{const.}, \tag{30}$$

thereby assuming again that all variables are constant across the layer. However, this ignores variations in the current, potential and concentrations along the CL. Therefore, deviations from this trivial scaling could be expected, similar in fashion to the results of the interface reduction of Section 3.4.

Fig. 8 shows that this first-order approximation is, in fact, a very good assumption. Numerical results, with $\overline{\eta}$ taken at the CL–GDL interface, coincide with Eq. (30). Here, *relative exchange current* refers to the reference case in Fig. 2. A variation of $i_{o,c}$ over four orders of magnitude is captured very well by the above approximation. This means that for standard operating conditions, the CL dynamics scale trivially with the exchange current and the layer can be described very well by the first-order approximation (30).

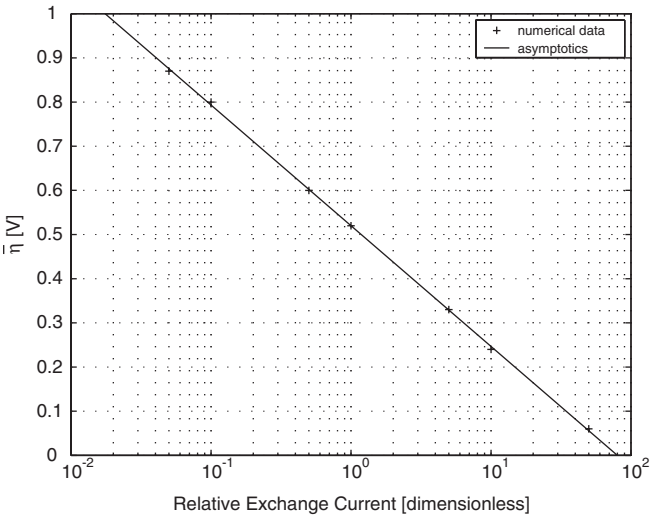

Fig. 8. Over-potential (taken at the CL–GDL interface) as a function of exchange current density relative to the reference case in Fig. 2. Only the exchange current density is varied; all other parameters as for the reference case.

3.6. Over-potential vs. ionomer hydration level

The local reaction rate $\overline{S}_c$ scales with the proton concentration like

$$\overline{S}_c \sim c_+^{e_c}, \tag{31}$$

where we chose $e_c = 1$ due to the dominating step of the overall reaction $O_2 + 4H^+ + 4e^- \rightarrow 2H_2O$. Therefore, we could again expect at first order that the over-potential, $\overline{\eta}(\bar{l})$, and proton concentration, $c_+(\bar{l})$, at the CL–GDL interface are related by

$$c_+ \exp\left(\frac{F\overline{\eta}}{2\mathscr{R}\overline{\tau}}\right) = \text{const.} \tag{32}$$

providing all other parameters, such as total current and CL–GDL oxygen concentration, remain fixed. In other words, only the proton concentration is varied and the over-potential changes in order to match the prescribed current.

Fig. 9 shows the over-potential as a function of the proton concentration, using the reference case and setting $c_w^m(0) = 1, 2, 3, \ldots, 14$. This prescribes c_+ via the ion exchange equilibrium $c_+ = c_+(c_w^m)$. Surprisingly enough, the numerical data points cannot be matched with the above lowest-order approximation for all c_+. Above $c_+ \approx 0.7$, or $c_w^m \approx 7.5$, it is well approximated for $e_c = 1$. For $c_+ < 0.7$, however, it is much closer to the $e_c = 2$ curve. It shall be pointed out though that $c_w^m < 3$, equivalent to $c_+ = 0.55$, corresponds to a very poorly humidified ionomer phase, usually unseen under normal operating conditions. Note that all three curves intersect at the reference case $c_w^m = 7.0$, where $c_+ \approx 0.69$, which is used as the starting point for the extrapolation.

When all boundary conditions are fixed and only $c_w^m(0)$ is varied, the nonlinearity in the problem causes the other variables to change. In this situation, (32) would hold if the water content had no impact on the oxygen concentration. However,

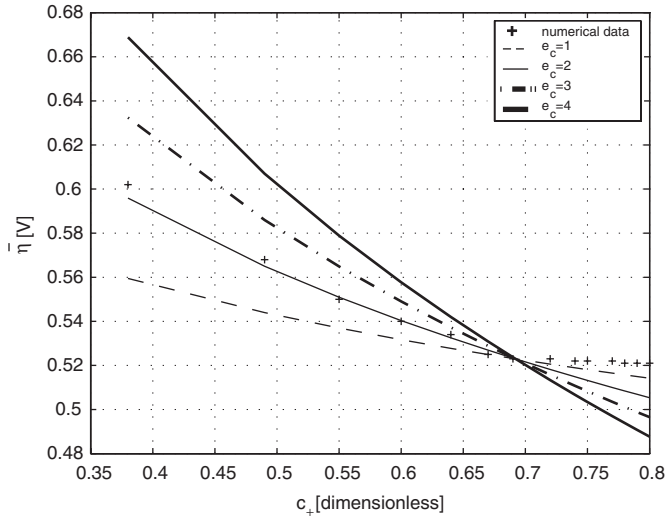

Fig. 9. Over-potential $\overline{\eta}$ (taken at the CL–GDL interface) as a function of the proton concentration c_+ at the CL–PEM interface. Although we use a value of $e_c = 1$ for the exponent of $\overline{c}_+$ in $\overline{S}_c$, the effective value is closer to 2 for poorly hydrated ionomers (small c_+) but approaches 1 for well-hydrated ionomers.

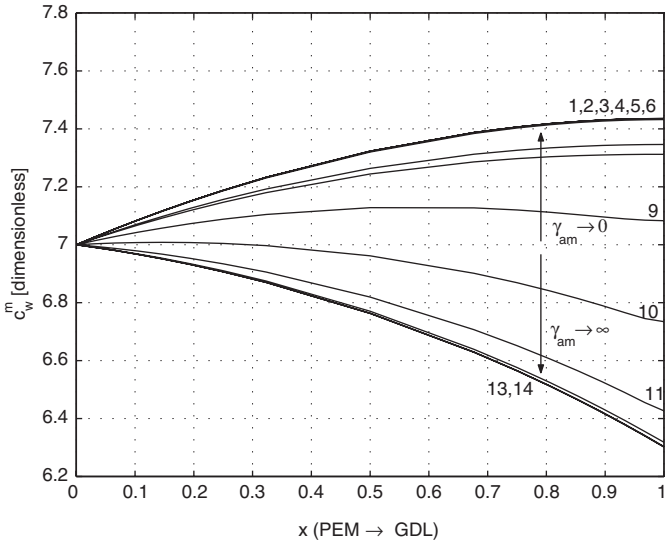

Fig. 10. There is a limiting ionomer water profile as the water uptake rate $\overline{\gamma}_{am}$ tends to ∞. However, while for small values of $\overline{\gamma}_{am}$ the no-flux boundary condition $\partial_x c_w^m(1) = 0$ is obviously met, large values of $\overline{\gamma}_{am}$ forces c_w^m to be near or at equilibrium in the interior. A boundary layer emerges at $x = 1$ of width $\sim 1/\sqrt{\overline{\gamma}_{am}}$, where the equilibrium does not hold but boundary conditions for both c_w^m and c_v can be met. Note: We vary $\overline{\gamma}_{am}$ from $5 \times 10^{-6}\,\mathrm{s}^{-1}$ (case 1) to $5 \times 10^{7}\,\mathrm{s}^{-1}$ (case 14), changing its value by a factor of 10 between successive cases.

it does have an impact through the binary gas flow in the pores and this is one reason for the variation. In some sense, adjusting e_c to make (32) hold is attempting to eliminate the impact of proton concentration on the reaction. The mismatch is enhanced by the variation of the ionomer water content c_w^m across the layer and, therefore, a variation of c_+.

This feature is again important when the CL is reduced to an interface for modelling purposes. In summary, the dependencies on the oxygen (Section 3.4) and proton concentrations in the Butler–Volmer equation, expressed by $\overline{S}_c$, can be expected to differ between a finite CL model and an interface model.

3.7. Asymptotic ionomer water profile for vanishing and infinite water uptake rates

Lastly, attention is drawn to the variation of the ionomer water profile with the water uptake rate coefficient $\overline{\gamma}_{am}$ (or γ_{am}, respectively). In the literature, this parameter is usually taken to be infinite (Siegel et al., 2004). This means that the ionomer, even under non-equilibrium ($I_t \neq 0$) fuel cell conditions, is at water sorption equilibrium, given by the isotherm (see Section 2)

$$\overline{c}_w^m = \overline{c}_w^*(\overline{\tau}, \overline{c}_v). \tag{33}$$

On the other hand, previous work by Berg et al. (2004) indicates that the equilibrium might not hold. However, that research was related to a unit cell model with a CL interface. Relating those results to the mass transfer coefficient $\overline{\gamma}_{am}$ in this work, which scales according to (9), is not a straightforward task. Due to this uncertainty in the estimation of $\overline{\gamma}_{am}$, we will study the variation of this parameter to understand its impact on the numerical results. We vary $\overline{\gamma}_{am}$ from $5 \times 10^{-6}\,\mathrm{s}^{-1}$ (case 1) to $5 \times 10^{7}\,\mathrm{s}^{-1}$ (case 14), changing its value by a factor of 10 between successive cases.

Fig. 10 shows how different values for $\overline{\gamma}_{am}$ affect the ionomer water profile. When $\overline{\gamma}_{am} \to 0$, the ionomer is effectively sealed and all water produced in the reaction remain in the ionomer. Hence, it must flow towards the PEM. Since the total current is prescribed, this determines the ionomer water flow at the CL–PEM interface. The water dynamics in the ionomer and the pores decouple and a limiting shape of c_w^m arises. The no-flux boundary condition $\partial_x c_w^m(1) = 0$ at the CL–GDL interface is obviously fulfilled, as one looks at the graph. As $\overline{\gamma}_{am}$ grows, this no-flux condition seems to be violated.

We also observe a limiting shape for $\overline{\gamma}_{am} \to \infty$. As shown in Appendix C, a boundary layer of width $\sim 1/\sqrt{\overline{\gamma}_{am}}$ emerges, in which the no-flux conditions (for $\overline{c}_w^m$ and $\overline{c}_v$, respectively) at either end are still met. When $\overline{\gamma}_{am}$ is large, the ionomer water content in the interior is near equilibrium, i.e., $\overline{c}_w^m \approx \overline{c}_w^*$. It is strongly coupled to the vapour concentration $\overline{c}_v$ in the pores and ultimately, as $\overline{\gamma}_{am} \to \infty$, it is entirely given by the local value of $\overline{c}_v$. The equilibrium holds everywhere except in the boundary layers. The emergence of one boundary layer for each concentration profile and the limiting shapes can be observed in Figs. 10 and 11 as $\overline{\gamma}_{am}$ increases from small values (1, 2, 3, 4, 5, 6) to larger values (9, 10). At very large values (11, 12, 13, 14), the boundary layer is too small to be visible in the plot. Note that $\overline{\gamma}_{am}$ is changed by one order of magnitude from one curve to the next.

We have used a non-uniform mesh to resolve the boundary layer. The boundary conditions are still met and there

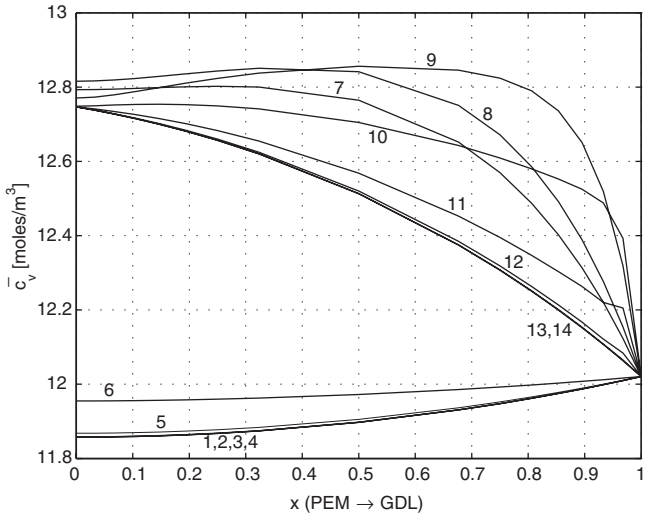

Fig. 11. The water vapour concentration with varying $\overline{\gamma}_{am}$. A limiting profile and a boundary layer (at $x = 0$) emerge as $\overline{\gamma}_{am} \to \infty$.

was no problem with respect to convergence. However, standardized commercial CFD codes do not provide the opportunity to choose a finite $\overline{\gamma}_{am}$. This leads to an arbitrarily small boundary layer, in which the boundary conditions can no longer be fulfilled and convergence issues might arise. Hence, the choice of infinite water uptake rate is not only unphysical but also causes major concerns during the numerical implementation.

4. Conclusions

This paper discussed a macroscopic model of a cathode CL in PEM fuel cells which describes the reaction–diffusion kinetics of this three-phase medium. The dynamics are governed by a large nonlinear system of differential equations which is very stiff. We presented a scaling and a numerical algorithm for solving efficiently this PDE system (see appendices), consisting of two imbedded Newton loops. The dynamics of the layer were investigated both numerically and analytically (asymptotically).

One key assumption was that the ionomer phase is not at water sorption equilibrium under steady-state fuel cell operation, which affects mainly the water balance between ionomer and pore within the layer. Water can both be adsorbed by the ionomer and evaporate into the pore along the layer. Another major assumption was that hydronium plays the sole role of ion transport within the ionomer. Governed by the local ion-exchange equilibrium, hydronium can be driven across the layer by the electric field against its concentration gradient.

In addition, diffusive losses for oxygen transport between pore and catalyst reaction sites lead naturally to maximum currents and the "knee" shape of the polarization curve. The maximum currents scale in a hyperbolic fashion with the transport parameter associated with this oxygen diffusion process. However, it does not exactly scale inverse proportional due to variations in current and other variables across the layer. Moreover, this explicit transport loss further amplifies the effect of maximum reaction rates near the GDL interface and a monotonic decline towards the PEM.

A main focus of this paper was to check the validity of the *interface reduction*, which is often used in large three-dimensional fuel cell computations and treats the CL as an interface. The results suggest that the interface reduction might not hold over the whole range of realistic oxygen concentrations or when liquid pore water is present. This is reflected by large variations in the effective exchange current density with operating conditions. This parameter takes the place of the exchange current density in the Butler–Volmer equation when the CL is treated as interfaces. By definition, only a constant effective exchange current density would allow for a successful interface reduction of the layer but its variation by one order of magnitude suggests otherwise.

Moreover, in the limit of infinite water sorption rate of the ionomer, a boundary layer emerges at either side of the CL, in which the water sorption equilibrium is violated. The thickness of this layer decreases with increasing water sorption rate. When the mesh is not refined in this boundary layer, the boundary conditions can no longer be met. This would explain why some commercial codes could fail to converge when applied to similar CL models using sorption isotherms. In addition, for both vanishing and infinite water sorption rates, the water profile in both the ionomer and the pore approach limiting shapes.

Acknowledgements

This work was supported by Ballard through the MITACS project Mathematical Modelling and Scientific Computation (MMSC). Peter Berg and Arian Novruzi are supported by NSERC Discovery Grants, Keith Promislow by NSF Grant 0345705.

Appendix A. The scaled model

Because of the numerical challenges related to the model with regard to its stiffness, a scaling of the model is necessary. This appendix presents briefly the procedure.

System (1)–(14), (25) subject to boundary conditions (24) has variables and physical constants varying over a large range of values, which in general leads to numerical instabilities. The system is transformed by scaling the space variable $\overline{x}$ and the CL so as to render the independent variables dimensionless, but keep the dependence of the equations on the dimensionless CL thickness l, as defined below, explicit.

The scalings for $\overline{\sigma}_{pm}$, $\overline{\gamma}_{am}$ and $\overline{\delta}$ are motivated by the fact that as $\overline{l} \to 0$, $\overline{\sigma}_{pm}$, $\overline{\gamma}_{am}$ must increase and $\overline{\delta}$ decrease, if the given current given by (25) has to be driven. For simplicity we

assume linear laws.

$$\begin{cases} x = \dfrac{\overline{x}}{\overline{l}}, & l = \dfrac{\overline{l}}{l_0},\ \ l_0 = 10^{-5}\,\mathrm{m}, \\ c_w^m(x) = \dfrac{1}{a}\overline{c}_w^m(\overline{x}), & \\ \varphi(x) = \dfrac{1}{E_0}\,\overline{\varphi}(\overline{x}), & E = \dfrac{E_0}{\eta^*},\ \ \eta^* = \dfrac{2\mathscr{R}\tau_r}{F}, \\ U(x) = \dfrac{1}{E_0}\,\overline{U}(\overline{x}), & \eta(x) = \exp\left(\dfrac{\overline{\eta}}{\eta^*}\right),\ \ \text{i.e.,} \\ & \overline{\eta}(\overline{x}) = \eta^* \ln(\eta + (\eta^2+1)^{1/2}), \\ \sigma_{pm} = \overline{l}\,\overline{\sigma}_{pm}, & \delta = \dfrac{1}{\overline{l}}\,\overline{\delta}, \\ \gamma_{am} = \overline{l}\,\overline{\gamma}_{am}, & \tau(x) = \dfrac{1}{\tau_*}\,(\overline{\tau}(\overline{x}) - \tau_r), \\ & \tau_* = \dfrac{a h_v \gamma_{am}}{\kappa_c} l_0, \\ & \tau_r = \text{given reference value}, \\ p(x) = \dfrac{1}{p_*}(\overline{p}(\overline{x}) - p_r), & p_* = \dfrac{a\mu\gamma_{am}}{K\mathbf{c}_r} l_0,\ \ p_r = \mathscr{R}\mathbf{c}_r\tau_r, \\ & \mathbf{c}_r = \dfrac{p_r}{\mathscr{R}\tau_r}, \\ c_v(x) = \dfrac{1}{\mathbf{c}_r}\,\overline{c}_v(\overline{x}), & c_o(x) = \dfrac{1}{\mathbf{c}_r}\overline{c}_o(\overline{x}). \end{cases} \tag{A.1}$$

From (15)–(23) and (A.1) it follows that

$$\begin{cases} \overline{c}_+ = a c_+, & c_+ := c_+(c_w^m) \\ & \quad = -\dfrac{k_H}{2}\,c_w^m + \left(\dfrac{1}{4}(k_H c_w^m)^2 + k_H c_w^m\right)^{1/2}, \\ \overline{S}_c = \dfrac{R_c}{l}\dfrac{c_+^{e_c} c_o \exp((F/2\mathscr{R}\overline{\tau})\overline{\eta})}{1 + \delta R_c^\delta c_+^{e_c}\exp((F/2\mathscr{R}\overline{\tau})\overline{\eta})} & R_c := \dfrac{\mathbf{c}_r}{l_0}\dfrac{\sigma_{pm} i_{0,c}}{F c_{o,\mathrm{ref}}}, \\ \quad \approx \dfrac{R_c}{l}\dfrac{c_+^{e_c} c_o \eta}{1 + R_c^\delta c_+^{e_c}\eta} & R_c^\delta := \dfrac{\sigma_{pm} i_{0,c}}{F c_{o,\mathrm{ref}}}\,\delta \ \text{(approaching } \overline{\tau} \text{ at } \tau_r), \\ \quad = \dfrac{R_c}{l} S_c, & S_c := \dfrac{c_o c_+^{e_c}\eta}{1 + R_c^\delta c_+^{e_c}\eta}, \\ \overline{I}_w = a(c_w^m - c_w^*) =: a I_w, & c_w^* = c_w^*(\tau, c_v) = \dfrac{1}{a}\overline{c}_w^*(\tau_r + \tau_*\tau, \mathbf{c}_r c_v) \\ & \quad = 0.3 + 10.8r - 16r^2 + 14.1r^3, \\ & r = \dfrac{\mathscr{R}\mathbf{c}_r}{101300} c_v(\tau_r + \tau_*\tau) 10^{-Q(\tau_r + \tau_*\tau)}. \end{cases} \tag{A.2}$$

Using the scalings (A.1) and (A.2), we can transform the governing equations contained within (1)–(14) as follows:

$$-\frac{\mathrm{d}}{\mathrm{d}x}\left(\frac{d_w e^{-2436/\overline{\tau}}}{l_0\gamma_{am}}\,c_w^m\frac{\mathrm{d}}{\mathrm{d}x}\,c_w^m\right) = l\frac{3R_c l_0}{2a\gamma_{am}}\,S_c - l(c_w^m - c_w^*(c_\tau, c_v)), \tag{A.3}$$

$$-\frac{\mathrm{d}}{\mathrm{d}x}\left(\frac{a}{R_c}\,\frac{d_+ e^{-1683/\overline{\tau}}}{l_0^2}\,c_w^m\left(\frac{F E_0}{\mathscr{R}\overline{\tau}}\,c_+\frac{\mathrm{d}}{\mathrm{d}x}\varphi + \frac{\mathrm{d}}{\mathrm{d}x}c_+\right)\right) = -l S_c, \tag{A.4}$$

$$-\frac{\mathrm{d}^2}{\mathrm{d}x^2}\tau = l\frac{\delta_s^c \tau_r R_c}{4\kappa_c\tau_*}\,l_0^2\left(\frac{\overline{\tau}}{\tau_r} + 4\frac{F\eta^*}{\delta_s^c\tau_r}\ln(\eta + (\eta^2+1)^{1/2})\right)S_c - l(c_w^m - c_w^*(\tau, c_v)), \tag{A.5}$$

$$-\frac{p_* K\mathbf{c}_r}{a\mu\gamma_{am}}\frac{1}{l_0}\frac{\mathrm{d}}{\mathrm{d}x}\left(\left(\frac{M_v - M_n}{M_v}c_v + \frac{M_o - M_n}{M_v}c_o + \frac{M_n}{M_v}\frac{1 + \frac{p_*}{p_r}p}{1 + \frac{\tau_*}{\tau_r}\tau}\right)\frac{\mathrm{d}}{\mathrm{d}x}p\right) = l(c_w^m - c_w^*(\tau, c_v)) - l\frac{M_o R_c l_0}{4M_v a\gamma_{am}}\,S_c, \tag{A.6}$$

$$-\frac{1}{a\gamma_{am}}\frac{1}{l_0}\frac{\mathrm{d}}{\mathrm{d}x}\left(\overline{D}_v\mathbf{c}_r\frac{\overline{\mathbf{c}}}{\mathbf{c}_r}\frac{\mathrm{d}}{\mathrm{d}x}\left(c_v\frac{\mathbf{c}_r}{\overline{\mathbf{c}}}\right) + \frac{K p_*\mathbf{c}_r}{\mu}c_v\frac{\mathrm{d}}{\mathrm{d}x}p\right) = l(c_w^m - c_w^*(\tau, c_v)), \tag{A.7}$$

$$-\frac{1}{a\gamma_{am}}\frac{1}{l_0}\frac{\mathrm{d}}{\mathrm{d}x}\left(\overline{D}_o\mathbf{c}_r\frac{\overline{\mathbf{c}}}{\mathbf{c}_r}\frac{\mathrm{d}}{\mathrm{d}x}\left(c_o\frac{\mathbf{c}_r}{\overline{\mathbf{c}}}\right) + \frac{K p_*\mathbf{c}_r}{\mu}c_o\frac{\mathrm{d}}{\mathrm{d}x}p\right) = -l\frac{R_c l_0}{4a\gamma_{am}}S_c, \tag{A.8}$$

$$-\frac{\overline{\sigma}_c E_0}{F R_c}\frac{1}{l_0^2}\Delta U = l S_c, \tag{A.9}$$

$$\ln(\eta + (\eta^2+1))^{1/2}) = E(1 - U + \varphi). \tag{A.10}$$

According to (25) and using the new variable x, the parameter φ_0 is chosen such that

$$F R_c\int_0^1 S_c\,\mathrm{d}x = F R_c\int_0^1 \frac{c_o c_+^{e_c}\eta}{1 + R_c^\delta c_+^{e_c}\eta}\,\mathrm{d}x = I_t. \tag{A.11}$$

Eqs. (A.3)–(A.10) are equipped with the boundary conditions (24) which in terms of dimensionless variables take the form

$$\begin{cases} c_w^m(0) = \dfrac{1}{a}\,\overline{c}_w^m(0) \ \text{ given}, & \dfrac{\mathrm{d}}{\mathrm{d}x}\,c_w^m(1) = 0, \\ \varphi(0) = \dfrac{\varphi_0}{E_0}, & \dfrac{\mathrm{d}}{\mathrm{d}x}\varphi(1) = 0, \\ \dfrac{\mathrm{d}}{\mathrm{d}x}\tau(0) = \alpha l\left(\dfrac{\tau_r}{\tau_*} + \tau\right), & \alpha = \overline{\alpha} l_0, \quad \tau(1) = \dfrac{\tau_r - \overline{\tau}(\bar{l})}{\tau_*} \ \text{ given}, \\ \dfrac{\mathrm{d}}{\mathrm{d}x}p(0) = 0, & p(1) = \dfrac{p_r - \overline{p}(\bar{l})}{p_*} \ \text{ given}, \\ \dfrac{\mathrm{d}}{\mathrm{d}x}c_v(0) = 0, & c_v(1) = \dfrac{\overline{c}_v(\bar{l})}{\mathbf{c}_r} \ \text{ given}, \\ \dfrac{\mathrm{d}}{\mathrm{d}x}c_o(0) = 0, & c_o(1) = \dfrac{\overline{c}_o(\bar{l})}{\mathbf{c}_r} \ \text{ given}, \\ \dfrac{\mathrm{d}}{\mathrm{d}x}U(0) = 0, & U(1) = \dfrac{\overline{U}(\bar{l})}{E_0} \ \text{ given}. \end{cases} \tag{A.12}$$

We will write the system of equations (A.3)–(A.12) in a more compact form as follows.

First, the following assumptions are made to simplify Eqs. (A.3)–(A.10). In (A.3)–(A.5), the variable $\overline{\tau}$ in the diffusion coefficient terms is replaced by τ_r. Moreover, in Eqs. (A.5)–(A.8) the terms τ_*/τ_r, p_*/p_r are assumed to be small and approximated by zero, the approximation $\frac{1+\tau(\tau_*/\tau_r)}{1+p(p_*/p_r)} = \overline{\mathbf{c}}/\mathbf{c}_r = 1$ is made. Moreover, it is convenient to introduce the following new parameters:

$$\begin{cases} D_w^m = \dfrac{d_w e^{-2436/\tau_r}}{l_0\gamma_{am}}, & r_c = \dfrac{3R_c l_0}{2a\gamma_{am}}, \\ D_+ = \dfrac{a}{R_c}\,\dfrac{d_+}{l_0^2}e^{-1683/\tau_r}, & D_\varphi = D_+\dfrac{FE_0}{\mathscr{R}\tau_r}, \\ \theta_r = \dfrac{\delta_s^c\tau_r R_c}{4\kappa_c\tau_*}l_0^2, & \theta_\eta = 4\dfrac{F\eta^*}{\delta_s^c\tau_r}, \quad \theta_p = \dfrac{M_o}{M_v}\,\dfrac{R_c l_0}{4a\gamma_{am}}, \\ u_r = \dfrac{p_* K\mathbf{c}_r}{a\gamma_{am}\mu}\dfrac{1}{l_0} = 1, & \\ m_v = \dfrac{M_v - M_n}{M_v}, & m_o = \dfrac{M_o - M_n}{M_v}, \quad m_n = \dfrac{M_n}{M_v}, \\ D_v = \dfrac{\overline{D}_v\mathbf{c}_r}{a\gamma_{am}}\dfrac{1}{l_0}, & D_o = \dfrac{\overline{D}_o\mathbf{c}_r}{a\gamma_{am}}\dfrac{1}{l_0}, \\ \sigma_c = \dfrac{\overline{\sigma}_c E_0}{FR_c}\dfrac{1}{l_0^2}, & E = \dfrac{E_0}{\eta_*}. \end{cases} \tag{A.13}$$

Next, let us set $\mathbf{v} = (v_1, \ldots, v_9) = (c_w^m, \varphi, \tau, p, c_v, c_o, U, \eta, \varphi_0)$ and according to Eqs. (A.3)–(A.11), we set

$$\mathbf{A}(\mathbf{v}) = \begin{bmatrix} D_w^m c_w^m & 0 & 0 & 0 & 0 & 0 & 0 & 0 & 0 \\ D_+ c_w^m \partial_{c_w^m} c^+ & D_\varphi c_w^m c_+ & 0 & 0 & 0 & 0 & 0 & 0 & 0 \\ 0 & 0 & 1 & 0 & 0 & 0 & 0 & 0 & 0 \\ 0 & 0 & 0 & m_v c_v + m_o c_o + m_n & 0 & 0 & 0 & 0 & 0 \\ 0 & 0 & 0 & c_v & D_v & 0 & 0 & 0 & 0 \\ 0 & 0 & 0 & c_o & 0 & D_o & 0 & 0 & 0 \\ 0 & 0 & 0 & 0 & 0 & 0 & \sigma_c & 0 & 0 \\ 0 & 0 & 0 & 0 & 0 & 0 & 0 & 0 & 0 \\ 0 & 0 & 0 & 0 & 0 & 0 & 0 & 0 & 0 \end{bmatrix},$$

$$\mathbf{S}(l, \mathbf{v}) = \mathbf{S}_0 + l\mathbf{S}_1 = \begin{bmatrix} 0 \\ 0 \\ 0 \\ 0 \\ 0 \\ 0 \\ 0 \\ \ln(\eta + (\eta^2+1)^{1/2}) - E(1 - U + \varphi) \\ FR_c\int_0^1 S_c\,\mathrm{d}x - I_t \end{bmatrix} + l\begin{bmatrix} r_c S_c - I_w \\ -S_c \\ \theta_r(1 + \theta_\eta \ln(\eta + (\eta^2+1)^{1/2}))S_c - I_w \\ -\theta_p S_c + I_w \\ I_w \\ -\dfrac{r_c}{6}S_c \\ S_c \\ 0 \\ 0 \end{bmatrix}.$$

For the boundary conditions (A.12), let $\mathbf{I}^0$, $\mathbf{I}^1$ be the 7×7 matrixes of zeros except $\mathbf{I}^0(i,i) = 1$, $i = 3, \ldots, 7$, $\mathbf{I}^1(i,i) = 1$,

$i = 1, 2$, and

$$\mathbf{b}^0(l, \mathbf{v}) = \mathbf{b}_0^0(\mathbf{v}) + l\mathbf{b}_1^0(\mathbf{v}) = \begin{bmatrix} \frac{1}{a}\overline{c}_w^m(0) - c_w^m(0) \\ \frac{\varphi_0}{E_0} - \varphi(0) \\ 0 \\ 0 \\ 0 \\ 0 \\ 0 \\ 0 \end{bmatrix} + l \begin{bmatrix} 0 \\ 0 \\ \frac{\tau_r}{\tau_*} + \tau(0) \\ 0 \\ 0 \\ 0 \\ 0 \\ 0 \end{bmatrix},$$

$$\mathbf{b}^1(\mathbf{v}) = \begin{bmatrix} 0 \\ 0 \\ \frac{\tau_r - \overline{\tau}(l)}{\tau_*} - \tau(1) \\ \frac{p_r - \overline{p}(l)}{p_*} - p(1) \\ \frac{\overline{c}_v(l)}{\mathbf{c}_r} - c_v(1) \\ \frac{\overline{c}_o(l)}{\mathbf{c}_r} c_o(1) \\ \frac{\overline{U}(l)}{E_0} - U(1) \\ 0 \end{bmatrix}.$$

Then Eqs. (A.3)–(A.12) are written as

$$-\frac{\mathrm{d}}{\mathrm{d}x}\left(\mathbf{A}(\mathbf{v})\frac{\mathrm{d}}{\mathrm{d}x}\mathbf{v}\right) = \mathbf{S}(l, \mathbf{v}) \quad \text{subject to} \tag{A.14}$$

$$\frac{\mathrm{d}}{\mathrm{d}x}\mathbf{I}^0\mathbf{v}(0) = \mathbf{b}^0(\mathbf{v}), \quad \frac{\mathrm{d}}{\mathrm{d}x}\mathbf{I}^1\mathbf{v}(1) = \mathbf{b}^1(\mathbf{v}). \tag{A.15}$$

Appendix B. Numerical solution

As $v_9 = \varphi_0$ defines a boundary condition for v_2, the solution of (A.14), (A.15) depends strongly on the parameter φ_0. The numerical solution is split into two steps: for a given v_9, find $\mathbb{v} = (\mathbb{v}_1, \ldots, \mathbb{v}_8)$, a solution of

$$\mathbb{L}(\mathbb{v}) := -\frac{\mathrm{d}}{\mathrm{d}x}\left(\mathbb{A}(\mathbb{v})\frac{\mathrm{d}}{\mathrm{d}x}\mathbb{v}\right) = -\mathbb{S}(l, \mathbb{v}) = 0, \quad \mathbb{A} \in \mathbb{R}^{8\times 8},$$
$$\mathbb{A}(i, j) = \mathbf{A}(i, j), \quad \mathbb{S} \in \mathbb{R}^8, \quad \mathbb{S}(i) = \mathbf{S}(i), \tag{B.1}$$

$$\frac{\mathrm{d}}{\mathrm{d}x}\mathbf{I}^0\mathbb{v}(0) = \mathbf{b}^0(\mathbb{v}), \quad \frac{\mathrm{d}}{\mathrm{d}x}\mathbf{I}^1\mathbb{v}(1) = \mathbf{b}^1(\mathbb{v}), \tag{B.2}$$

and, thereafter, update v_9 for solving $E(\mathbb{v}) := FR_c\int_0^1 S_c(\mathbb{v})\,\mathrm{d}x - I_t = 0$. Thus, $\mathbb{v} = \mathbb{v}(v_9)$.

Let $\mathbb{V} = (v_1, \ldots, v_8)$ be the space of functions satisfying (B.2) (it is an affine space). Then, the problem is to find v_9 such that

$$E(\mathbb{v}) = 0 \quad \text{with } \mathbb{L}(\mathbb{v}) = 0, \quad \mathbb{v} = \mathbb{v}(v_9) \in \mathbb{V}. \tag{B.3}$$

We use the following classical Newton's method to solve numerically problem (B.3):

(1) $n = 0$. Choose v_9^n.
(2) Update v_9^n using Newton's method

$$v_9^{n+1} = v_9^n - \frac{E(\mathbb{v}^n)}{\partial_{v_9}E(\mathbb{v}^n)} = v_9^n - \frac{E(\mathbb{v}^n)}{\partial_{\mathbb{v}}E(\mathbb{v}^n)(\partial_{v_9}\mathbb{v}^n)},$$
$$\mathbb{v}^n = \mathbb{v}(v_9^n). \tag{B.4}$$

In order to evaluate (B.4), we need to compute:
(a) $\mathbb{v}^n$, which satisfies

$$\mathbb{L}(\mathbb{v}^n) = 0, \quad v_2^n(0) = v_9^n, \quad \mathbb{v}^n \in \mathbb{V}. \tag{B.5}$$

As (B.5) is a nonlinear differential system of equations, in practice we solve it approximately using Newton's method. For $v_9 = v_9^n$, solve $\mathbb{v}^n$ approximately by:
(a.1) $m = 0$. Choose $\mathbb{v}^{n,m}$.
(a.2) Update $\mathbb{v}^{n,m}$

$$\mathbb{v}^{n,m+1} = \mathbb{v}^{n,m} - [\partial_{\mathbb{v}}\mathbb{L}(\mathbb{v}^{n,m})]^{-1}\mathbb{L}(\mathbb{v}^{n,m}),$$
$$v_2^{n,m+1}(0) = v_9^n, \quad \mathbb{v}^{n,m+1} \in \mathbb{V}. \tag{B.6}$$

(a.3) If $\|\mathbb{v}^{n,m+1} - \mathbb{v}^{n,m}\| < \varepsilon$, take $\mathbb{v}^n = \mathbb{v}^{n,m}$ and goto (b); else goto (a.2).

(b) $\partial_{\mathbb{v}}E(\mathbb{v}^n)(\partial_{v_9}\mathbb{v}^n)$, which requires computation of $\partial_{v_9}\mathbb{v}^n$, a solution of the linear differential system of equations

$$\partial_{\mathbb{v}}\mathbb{L}(\mathbb{v}^n)(\partial_{v_9}\mathbb{v}^n) = 0, \quad \text{subject to}$$
$$\frac{\mathrm{d}}{\mathrm{d}x}\mathbf{I}^0\partial_{v_9}\mathbb{v}^n(0) = \partial_{v_9}\mathbf{b}^0(\mathbb{v}^n)(\partial_{v_9}\mathbb{v}^n),$$
$$\frac{\mathrm{d}}{\mathrm{d}x}\mathbf{I}^1\partial_{v_9}\mathbb{v}(1) = \partial_{v_9}\mathbf{b}^1(\mathbb{v}^n)(\partial_{v_9}\mathbb{v}^n). \tag{B.7}$$

The boundary conditions for $\partial_{v_9}\mathbb{v}^n$ are obtained from (A.15), by differentiating both sides of the equations with respect to $v_9 = \varphi_0$.

(3) If $|v_9^{n+1} - v_9^n| + |E(\mathbb{v}^n)| < \varepsilon$ stop; else go to (1).

Remark B.1. In our numerical computations Eq. (B.6) is solved approximately using a finite element method (Ciarlet, 2002). Let us first point out that (B.6) is equivalent to

$$\partial_{\mathbb{v}}\mathbb{L}(\mathbb{v}^{n,m})(\delta^{n,m}) = -\mathbb{L}(\mathbb{v}^{n,m}),$$
$$\delta^{n,m} \in \mathbb{V}, \quad \mathbb{v}^{n,m+1} = \mathbb{v}^{n.m} + \delta^{n,m}. \tag{B.8}$$

Several terms of $\mathbb{L}(\mathbb{v}^{n,m})$ are nonlinear in terms of $\mathbb{v}^{n,m}$, so an appropriate approximation $\mathbb{L}_h$ of $\mathbb{L}$ is considered instead. Moreover, if $\{x_0, \ldots, x_N\}$ is a discretization of $[0, 1]$ and ξ_i, $i = 0, \ldots, N$, are the usual hat functions, we look for $\delta_h^{n,m} \in \mathbb{V}_h := \mathbb{V} \cap \mathrm{span}\{\xi_1, \ldots, \xi_N\}$, solution of

$$\int_0^1 \partial_{\mathbb{v}}\mathbb{L}_h(\mathbb{v}_h^{n,m})(\delta_h^{n,m})\xi_i = -\int_0^1 \mathbb{L}_h(\mathbb{v}_h^{n,m})\xi_i,$$
and so $\mathbb{v}_h^{n,m+1} = \mathbb{v}_h^{n,m} + \delta_h^{n,m}$.

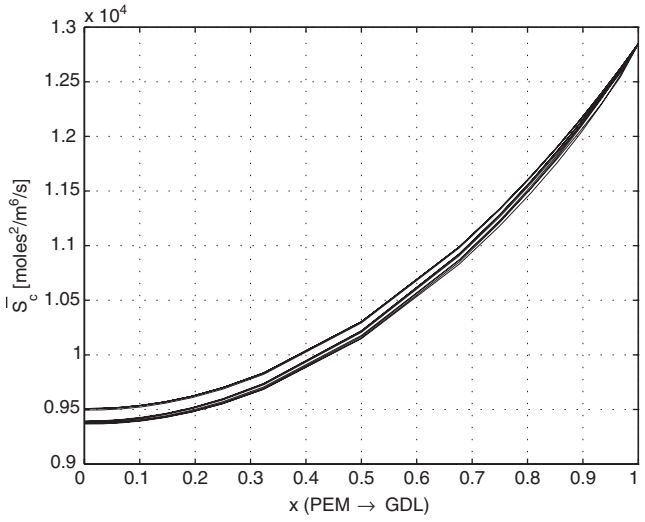

Fig. 12. Local reaction rate $\overline{S}_c$ with varying $\overline{\gamma}_{am}$, corresponding to Figs. 10 and 11. The variation in all cases is smaller than 35% and assumed to be constant for the boundary layer analysis.

Remark B.2. The system of differential equations (B.7) is linear; it is solved approximately using the finite element method. At step n the approximation $\partial_{v_9}\mathbb{v}_h^n \in \mathbb{V}_h$ of $\partial_{v_9}\mathbb{v}^n$ is a piecewise linear vector function satisfying

$$\int_0^1 \partial_{\mathbb{v}}\mathbb{L}_h(\mathbb{v}_h^n)(\partial_{v_9}\mathbb{v}_h^n)\xi_i = 0.$$

Appendix C. Water sorption equilibrium and boundary layer analysis

In this appendix, we present a simplified toy model that describes qualitatively the emergence of a boundary layer as the deviation from water sorption equilibrium vanishes in the interior of the layer. This corresponds to the limit of an infinitely large water uptake rate, $\overline{\gamma}_{am} \to \infty$.

The deviation from the water sorption isotherm is expressed by the term

$$\overline{I}_w = \overline{c}_w^m - \overline{c}_w^*. \tag{C.1}$$

We assume to lowest order that temperature, pressure, and local reaction rate (Fig. 12) are constant throughout the layer. We consider now linear diffusion of ionomer water due to small variation in $\overline{c}_w^m$ and, therefore, $\overline{D}_w$. We also choose a linear water sorption isotherm

$$c_w^* = \overline{c}_w^*(\overline{\tau}, \overline{c}_v) = \beta\overline{c}_v, \tag{C.2}$$

which is again justified by small variations of $\overline{c}_v$ throughout the layer and rescaling of $\overline{c}_w^m$. For our purposes, we set $\beta = 1$. Also, $\overline{c}_v$ is dominated by diffusion. This results in a toy model with two equations for the ionomer water and pore vapour concentrations. From (1), (11), they have the qualitative form ($I := 3\overline{S}_c/2$, $w = \overline{c}_w^m$, $v = \overline{c}_v$)

$$-\overline{D}_w w_{\overline{x}\overline{x}} = -\overline{\gamma}_{am}(w - v) + I, \tag{C.3}$$

$$-\overline{D}_v v_{\overline{x}\overline{x}} = \overline{\gamma}_{am}(w - v). \tag{C.4}$$

Division by $\overline{D}_w$ and $\overline{D}_v$, respectively, followed by subtraction yields

$$(w - v)_{\overline{x}\overline{x}} = \gamma(w - v) - I^* \tag{C.5}$$

with

$$\gamma = \overline{\gamma}_{am}\left(\frac{1}{\overline{D}_w} + \frac{1}{\overline{D}_v}\right) \quad \text{and} \quad I^* = \frac{I}{\overline{D}_w}. \tag{C.6}$$

This can be solved easily and we obtain for the deviation from sorption equilibrium, $w - v$,

$$w - v = A\exp(\sqrt{\gamma}\overline{x}) + B\exp(-\sqrt{\gamma}\overline{x}) + \frac{I^*}{\gamma}. \tag{C.7}$$

The constants A and B are given by the boundary conditions at $\overline{x} = 0$ and $\overline{l}$, respectively. Following the no-flux and Dirichlet conditions of the model in this work, we find

$$w(0) = \overline{c}_w^o, \quad w_{\overline{x}}(\overline{l}) = 0, \tag{C.8}$$

$$v_{\overline{x}}(0) = 0, \quad v(\overline{l}) = \overline{c}_v^o. \tag{C.9}$$

We see that as $\overline{\gamma}_{am} \to \infty$, i.e., $\gamma \to \infty$, two boundary layers form at either end of the layer, having thickness $\delta_{bc} = 1/\sqrt{\gamma}$. They emerge because the system is forced increasingly closer to equilibrium, i.e., $I^*/\gamma \to 0$, in the interior while at the boundary, a no-flux condition of one phase is faced by a non-vanishing flux in the other phase.

Note that the water produced in the reaction in the interior of the layer must flow out of the layer at steady state. Hence, the boundary conditions can only be met simultaneously, if the sorption equilibrium does not hold in the boundary layers. Otherwise, we would find $w \equiv v$ throughout the layer and $w_{\overline{x}}(\overline{l}) = 0$ would imply $v_{\overline{x}}(\overline{l}) = 0$ and, likewise, $v_{\overline{x}}(0) = 0$ would imply $w_{\overline{x}}(0) = 0$. This would contradict the production of water in the interior which must flow out of the domain.

References

Berg, P., Promislow, K., St-Pierre, J., Stumper, J., Wetton, B., 2004. Water management in PEM fuel cells. Journal of the Electrochemical Society 151, A341–A353.

Berg, P., Promislow, K., Stumper, J., Wetton, B., 2005. Discharge of a segmented PEM fuel cell. Journal of Fuel Cell Science and Technology 2, 111–120.

Ciarlet, P.G., 2002. The finite element method for elliptic problems. SIAM Classics in Applied Mathematics, No. 40, SIAM, Philadelphia.

Eikerling, M., 2006. Water management in cathode catalyst layers of PEM fuel cells: a structure-based model. Journal of the Electrochemical Society 153 (3), E58–E70.

Eikerling, M., Kornyshev, A., Kulikovsky, A., 2005. Can theory help to improve fuel cells? Fuel Cell Review (January Issue) 15–24.

Litster, S., McLean, G., 2004. PEM fuel cell electrodes. Journal of Power Sources 130, 61–76.

Paddison, S., Paul, R., Zawodzinski, T., 2000. A statistical mechanical model of proton and water transport in a proton exchange membrane. Journal of the Electrochemical Society 147, 617–626.

Pisani, L., Valentinin, M., Murgia, G., 2003. Analytical pore scale modeling of the reactive regions of polymer electrolyte fuel cells. Journal of the Electrochemical Society 150, A1549–A1559.

Serfass, J., Bergman, M., Rodenhiser, W., 1994. Commercial, environmental and legislative factors that influence the implementation of fuel cells. Journal of Power Sources 49, 193–208.

Siegel, N., Ellis, M., Nelson, D., Spakovsky, M., 2004. A two-dimensional computational model of a PEMFC with liquid water transport. Journal of Power Sources 128, 173–184.

Song, D., Wang, Q., Liu, Z., Navessin, T., Eikerling, M., Holdcroft, S., 2004. Numerical optimisation study of catalyst layer for PEM fuel cell cathode. Journal of Power Sources 126, 104–111.

Stumper, J., Haas, H., Granados, A., 2005. In situ determination of MEA resistance and electrode diffusivity of a fuel cell. Journal of the Electrochemical Society 152, A837–A844.

Wang, Q., Eikerling, M., Song, D., Liu, Z., 2004. Structure and performance of different types of agglomerates in cathode catalyst layers of PEM fuel cells. Journal of Electroanalytical Chemistry 573, 61–69.

Zawodzinski, T., Derouin, C., Radzinski, S., Sherman, R., Smith, V., Springer, T., Gottesfeld, S., 1993. A comparative study of water uptake by and transport through ionomeric fuel cell membranes. Journal of the Electrochemical Society 140, 1981–1985.